Acta Materialia 131 (2017) 499–510

Contents lists available at ScienceDirect

Acta Materialia

journal homepage: www.elsevier.com/locate/actamat

Full length article

Microstructure evolution and superelastic behavior in Ti-35Nb-2Ta-3Zr alloy processed by friction stir processing

Liqiang Wang [a, *], Lechun Xie [a], Yuting Lv [a], Lai-Chang Zhang [b], Liangyu Chen [c], Qiang Meng [d], Jiao Qu [a], Di Zhang [a], Weijie Lu [a, *]

[a] State Key Laboratory of Metal Matrix Composites, Shanghai Jiao Tong University, Shanghai, 200240, China
[b] School of Engineering, Edith Cowan University, 270 Joondalup Drive, Joondalup, Perth, WA, 6027, Australia
[c] School of Science, Jiangsu University of Science and Technology, Zhenjiang, Jiangsu, 212003, China
[d] Beijing FSW Technology Co.Ltd, No.1 Dongjunzhuang, Chaoyang District, Beijing, 100024, China

ARTICLE INFO

Article history:
Received 25 November 2016
Received in revised form
9 March 2017
Accepted 11 March 2017
Available online 8 April 2017

Keywords:
Friction stir processing
Surface modification
Martensitic phase transformation
Mechanical property

ABSTRACT

This work investigates systematically the phase transformation and superelasticity in TiNbTaZr alloy prepared by friction stir processing (FSP). Multiple-pass FSP with a 100% accumulated overlap to three passes was implemented. The influence of the processing parameters on the microstructural evolution and superelasticity in stir zone, transition zone, and heat affected zone were investigated. After recrystallization, existing dislocations gradually accommodate themselves at sub-grain boundaries. Increase in the proportion of α'' martensitic phase is always accompanied by significant reduction in the fraction of ω phase precipitation. Metastable ω phase dissolving feature is evident and promoted by dislocation gliding, especially in the specimen processed at a higher rotation speed. In nanoindentation measurements, the closer the indent applied towards the transition zone, the more martensites nucleate, thereby gradually reducing both elastic modulus and hardness *via* re-orientation of martensites. This study provides new insight into the surface modification of beta titanium alloys through FSP method to achieve improved mechanical properties.

1. Introduction

Recently, β-type titanium alloys have been increasingly considered as excellent implant materials because of the remarkable combination of high strength-to-weight ratio, good fatigue resistance, relatively low Young's modulus, good biocompatibility and high corrosion resistance [1–3]. Compared to the conventional (α+β)-type titanium biomaterials such as Ti-6Al-4V, β-type titanium alloys containing non-toxic constituents possess Young's modulus (~60 GPa) closer to that of bone (10–30 GPa). From the viewpoint of practical biomedical application, it is highly desirable to obtain superelasticity for β-type titanium alloys at higher strain rates or lower temperatures. It is also important to fully understand the superelastic behavior in β-type titanium alloys. In the past few years, extensive endeavors have been made to produce β-type titanium alloys with a high superelasticity performance [4,5]. For the commonly studied Ti-Nb alloys, superelastic effect is attributed to the reducing proportion of β stabilizing elements such as Ta or Nb [4]. To our knowledge, increasing critical stress for slip deformation can also improve the superelasticity. For instance, precipitation hardening effect *via* fine ω phase and solid solution strengthening after cold rolling both enhance critical stress for slip deformation, which improves the superelasticity significantly [6,7]. Therefore, there is no doubt that nanostructured and ultrafine-grained titanium alloys would exhibit better superelastic performance.

According to present literature, ultrafine-grained or nanostructured titanium alloys could be obtained through severe plastic deformation [8–18]. For example, Yilmazer et al. [12,13] found that high-pressure torsion (HPT) results in fine microstructure in precipitation-hardened Ti-29Nb-13Ta-4.6Zr (TNTZ) β-type titanium alloy thereby enhancing its hardness. Currently, extensive studies are being focused on the surface modification, composition manipulations, heat treatment, and composites reinforced by hard precipitates to improve the mechanical properties of titanium alloys [19–24]. As one of SPD methods [25], friction stir processing (FSP), a novel solid-state surface modification technique, is emerging as a very attractive method of localizing thermom-

* Corresponding authors.
E-mail addresses: wang_liqiang@sjtu.edu.cn (L. Wang), luweijie@sjtu.edu.cn (W. Lu).

http://dx.doi.org/10.1016/j.actamat.2017.03.079
1359-6454/

echanical processing. Two main processing parameters in FSP, i.e. rotation speed and pass number, significantly influence the microstructure of the processed materials. Increasing pass number during FSP can refine grains due to severe plastic deformation experienced and severe stirring effect in stir zone, which significantly optimized surface properties [26]. Multiple-pass FSP with a 100% overlap was reported to be an effective approach to achieve refined and homogeneous microstructure in as-cast AZ91 [27]. Currently, FSP has been increasingly applied for surface modification of Ti-6Al-4V alloy [28]. However, very few studies on solid-state surface modification towards β-type titanium alloys and associated phase transformation mechanism have been reported.

In the past few years, different kinds of phase transformation mechanisms have evolved into a key goal in research related to β-type titanium alloys. To that effect, research efforts have resulted in a number of means that are actively being pursued. For instance, dislocation slipping, stress-induced α″ martensite phase transformation and deformation twins were reported in cold-deformed beta titanium alloy [29]. During equal channel angular pressing, strain induced excessive dislocation tangles and defects in grain or subgrain boundaries and interiors play detrimental roles in phase transformation driven process, causing more martensite nucleation than martensite propagation [11]. However, ω phase precipitation was little observed in the aforementioned work. Owing to different microstructural features, such as stacking faults and dislocations generated during FSP, ω and α″ martensite phase transformation is different from those in titanium alloys prepared by other severe plastic deformation technologies as reported in Refs. [11,29–33].

In this work, FSP method was employed for surface modification of the newly-developed Ti-35Nb-2Ta-3Zr (wt%) alloy with a low Young's modulus of approximately 48 GPa [29–31]. This work systematically investigated the effect of FSP on the phase transformation and mechanical properties of Ti-35Nb-2Ta-3Zr alloy. α″ martensite phase, ω phase transformation characteristics and associated nucleation mechanism were detailed discussed. The superelasticity associated with martensite phase transformation in stir zone was also explored *via* nanoindentation tests. This study provided a new insight into the surface modification of β-type titanium alloys through FSP method to obtain desired mechanical properties for biomedical applications.

2. Experimental

2.1. Material preparation

Pure elemental constituents with 99.5 wt% purity were arc-melted under an argon atmosphere to form Ti-35Nb-2Ta-3Zr alloy. The ingot was melted three times for chemical homogeneity. As-cast ingot was homogenized at 1223 K for 1 h in vacuum condition and then forged into a billet with 40 mm in diameter and 160 mm in length. Afterward, the billet was solution treated at 780 °C for 30 min followed by air cooling. Finally, the solutionized Ti-35Nb-2Ta-3Zr billet was rolled into a sheet about 5 mm in thickness, with the total rolling reduction ratio about 90% with a reduction ratio about 5% for each pass at room temperature. In order to eliminate rolling stress and obtain homogeneous β phase, solid solution treatment was carried out at 780 °C for 30 min, followed by air cooling.

2.2. Friction stir processing

Friction stir processing was performed using a professional FSW machine with a FSP tool of tungsten steel. Probe diameter and probe plunge depth used during FSP were 10.0 mm and 2.0 mm respectively. During FSP procedures, argon was introduced surrounding both rotating tool and surface layers of FS-processed zones with aim to prevent high temperature oxidation of Ti-35Nb-2Ta-3Zr alloy. The processing parameters were at a constant travel speed of 50 mm/min at rotation speed of 225 and 300 r/min. Multiple-pass FSP with a 100% accumulated overlap to three passes was implemented for further grain refinement. Fig. 1 indicates the schematic view of friction stir process.

2.3. Microstructural observations

FSPed samples for metallographic examinations were cut, ground, polished, and etched in a solution containing 10 vol% HF, 30 vol% HNO_3, and 60 vol% H_2O. Microstructure observations were carried out by transmission electron microscopy (TEM) and high resolution TEM (HRTEM) with a JEM2100 microscope operating at 200 kV. TEM specimens were sampled from stir zone and twin-jet polished in a solution with 3 vol% perchloric acid and 97 vol% alcohol at −25 °C. The observed area posses the same thickness around 100 nm for each TEM sample. Specimen with 10 mm in length, 10 mm in width and 4 mm in height was cut from Ti-35Nb-2Ta-3Zr alloy, and then ion polished for 4–5 h in Gatan Model 693 Precision Cross Section System for Electron backscattered diffraction (EBSD) characterization in a Nova FEI 400 field emission scanning electron microscope (SEM) equipped with HKL Channel Oxford 5 EBSD system. The microscope was operated at 20 kV and 8 nA with the stage tilted at an inclination of 70°. The specimen was scanned at a scan step size of 1 μm and a spot size of 5 nm. The grain tolerance angle used for grain-size measurements was 5°, and lower limit boundary-misorientation cutoff was 2° for misorientation measurements. The EDS detector was fully retracted to avoid overexposure due to the large current used to collect the EBSD data.

2.4. Nanoindentation tests

Nanoindentation measurements were performed using an NANO Indenter G200 Tester device which employs a lock-in technique for determination of the indentation-depth-dependent mechanical properties at the same position on the sample in the course of a single loading-unloading curve. In the case of the different superelasticity, it was possible to perform several different indentations from the top surface in stir zone at the different location considering each test independently from others. To perform several cycles in a reproducible and comparable way, three identical loading and unloading cycles were conducted with the equal maximum load and constant applied loading rate in the location with the same depth to the surface. Nanoindentation tests were carried out at room temperature using a nanoindenter with a

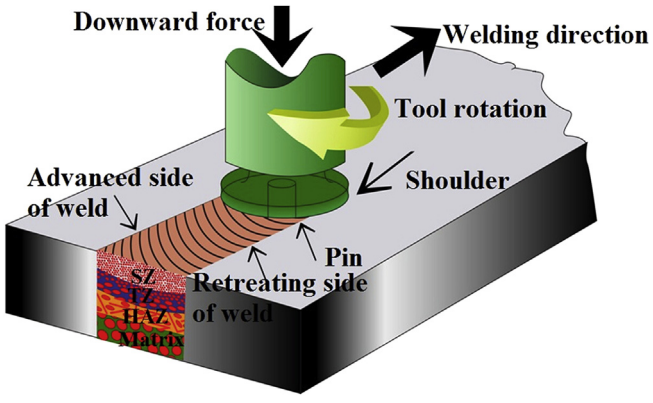

Fig. 1. Schematic view of friction stir process.

Berkovich tip at continuous load up to a maximum value of 50 mN with a loading rate of 1.0 mN/s. Before unloading step performed at a rate of 1.0 mN/s, a 5s dwelling time was applied at maximum load about 50 mN. Indentations were operated at sufficiently large distance from each other to avoid any interaction between stress fields generated by the indentation and the elastic incompatibility stresses associated to the presence of a grain boundary. The distance between each individual indent was around 30 μm to ensure that the value of each indent was accurate without any surface modification effect by others.

3. Results

3.1. Microstructure characteristics

Fig. 2 shows the SEM micrographs of distinct regions in transversal cross-section of three-pass FSPed samples. Four distinct regions can be consecutively observed from the upper surface of FSP zone as marked in Fig. 2(a), i.e. stir zone (SZ), transition zone (TZ), heat affected zone (HAZ) and base metal (BM or matrix). The principal directions in Fig. 2(a) are identified as WD (welding direction), TD (transverse direction) and ND (normal direction) of the specimen, which are the same as indicated in other reports (e.g. Refs. [34–39]).

SEM observations have indicated no distinct difference in morphology for regions A-E in the SZ. The characteristics of the SZ include uniform equiaxed fine grains in hundreds of nanometers (Fig. 2(b)), which are much finer than the grains in matrix with a size of 50 μm (Fig. 2(e)). Meanwhile, many cavities induced by grain boundary sliding are distinctly observed in the SZ (Fig. 2(b)). Fig. 2(c) shows the typical microstructure for the TZ, which includes shear bands together with elongated grains along transverse direction. Extensive grain boundary sliding along with somewhat elongated grains is observed (Fig. 2(c)). As clearly indicated in the enlarged region marked by the square, coarser gains without second phase are distinct in TZ in comparison with SZ. Furthermore, less cavities are observed in TZ, which is especially indicated by extensive grain boundary sliding and remarkable grain elongation.

Different from the microstructure in SZ and TZ, massive lentoid laths with an average length of 100 μm are visible in the region H in HAZ, as marked in Fig. 2(d). According to our knowledge, HAZ experiences a thermal cycle, but does not undergo any plastic deformation. It is also reported that martensitic transformation could be induced under applied force such as high pressure torsion and one dimensional shock loading [40,41]. It is known that during friction stir processing, high plunge depth results in high forces perpendicular to the friction stir processed surface, which ultimately induces the martensitic transformation as observed above. The morphology and distribution of martensites in HAZ are significantly different compared to those in SZ and TZ.

Fig. 3 shows the EBSD microstructural features of equiaxed grains in SZ and TZ. As seen from Fig. 3(a) and (b), SZ consists of grains with average size of about 0.9 μm, indicating that recrystallization has occurred in SZ. Fig. 3(c) shows the misorientation angle distribution, which indicates the fraction of high angle grain boundaries (HAGBs) in SZ is 88.7%. Such a high fraction of HAGBs with an average misorientation angle of 36.2° implies the occurrence of dynamic recrystallization (DRX) resulting from severe plastic deformation during three-pass FSP. Compared with the microstructure evolution in SZ, relatively coarser grains are observed in TZ, which have a grain size of around 1.2 μm (Fig. 3(e)). Meanwhile, the fraction of HAGBs in TZ is 76.4% and the average misorientation angle is 31.4° (Fig. 3(f)). It has commonly been reported that boundary migration would contribute much to DRX, especially in those materials with high stacking fault energy, such as Ti–6Al–4V during severe plastic deformation at high temperature [42]. In this work, a large number of micron-sized new grains are formed in SZ. As such, the boundary misorientation will be promoted gradually. In addition, the black-colored areas in EBSD maps in Fig. 3(a) and (d) indicate the appearance of cavities, which cannot be identified as newborn phases. Compared with TZ, much more black color areas in SZ thus mean more cavities in SZ, which is consistent with the SEM observations in Fig. 2(b).

Fig. 4(a) shows the optical microstructure for the cross-section of the three-pass FSP-processed samples at the rotation speed of 225 r/min, which reveals a depth of about 1655.75 μm in stir zone. Fig. 4 (b)-(f) are the TEM images of upper stir zone (i.e. the region A in Fig. 4(a)). The grains in upper stir zone are homogeneously refined and have a size less than 1 μm (Fig. 4(b)). Meanwhile, no distinct anisotropy is observed for recrystallized grains in upper region near the top surface. Dislocation tangles are clearly presented around recrystallized grains (Fig. 4(c)). This scenario is similar to the previous report that high density dislocations are especially found around grain boundaries [43]. Fig. 4(d) shows the precipitation of α″ martensitic phase. Needle-shape martensitic laths with about 500 nm in length and less than 100 nm in width are formed inside recrystallized grains. In addition, ω phase is also present inside the grains. Fig. 4(e) and (f) show both the bright- and dark-field images of ω phase, respectively. The corresponding selected area electron diffraction (SAED) pattern with distinct ω phase spots in Fig. 4(f) shows that ω phase are induced during FSP in the upper region of stir zone and that the orientation relationship between β matrix and ω phase is $[1\bar{1}1]_\beta // [11\bar{2}0]_\omega$.

The bright-field image shown in Fig. 5 displays the details of the deformation twins taken from the same region (region A, as marked in Fig. 4(a)). Plate shaped deformation twins coupled with ω phase are also observed in Fig. 5(a). The zone axis of the SAED pattern is parallel to the $[011]_\beta$ direction, which is taken from the same region as marked in Fig. 5(a). It has been reported that $\{332\}_\beta\langle 113\rangle_\beta$ and $\{112\}_\beta\langle 111\rangle_\beta$ twins are regularly observed in the metastable β-type titanium alloys [44–46]. In this work, the twins are identified as $\{332\}_\beta\langle 113\rangle_\beta$. Fig. 5(b) shows the indexed diagram corresponding to β matrix, β twin, and ω phase.

Regarding the microstructure evolution in region B marked in Fig. 4(a), inhomogeneous recrystallized grains are presented in the middle stir zone, with sizes of 0.5–1 μm in diameter (Fig. 6 (a)). Elongated grains extending along welding direction are also observed accompanying equiaxed grains. Meanwhile, dislocation tangles take place around grain boundaries of some recrystallized grains (Fig. 6 (b)). Compared with the morphologies of upper stir zone (Fig. 4), relatively smaller grains and more dislocations around the recrystallized grains are evident in the middle stir zone. Such a change in grain size is associated with the differences in temperature profile and in heat dissipation in stir zone during FSP. In the middle stir zone, the peak temperature is lower and the thermal cycle is shorter compared to the nugget top. The combination of lower temperature and shorter excursion time at the middle stir zone effectively restrains grain growth thereby refining recrystallized grains [47]. This result is similar to the findings that grains in stir zone tend to grow near top surface [48]. The stress-induced α″ nucleates and grows quickly in the middle stir zone inside the recrystallized grains, leading to the formation of long stress-induced α″ martensites (Fig. 6(c)). As illustrated in Fig. 6(c), stress-induced α″ martensite is favored in region B. The SAED pattern in Fig. 6(c) inset specifies clearly the relation between α″ martensitic phase and ω phase, showing the precipitation of α″ phase. Fig. 6(d) and (e) show the bright-field and dark-field images of ω phase, respectively. HRTEM image of domain A in (d) along $\langle 1\bar{1}1\rangle_\beta$ zone axis shows the boundary between ω phase and β phase. As seen from the HREM image (Fig. 6(f)), the direct evidence

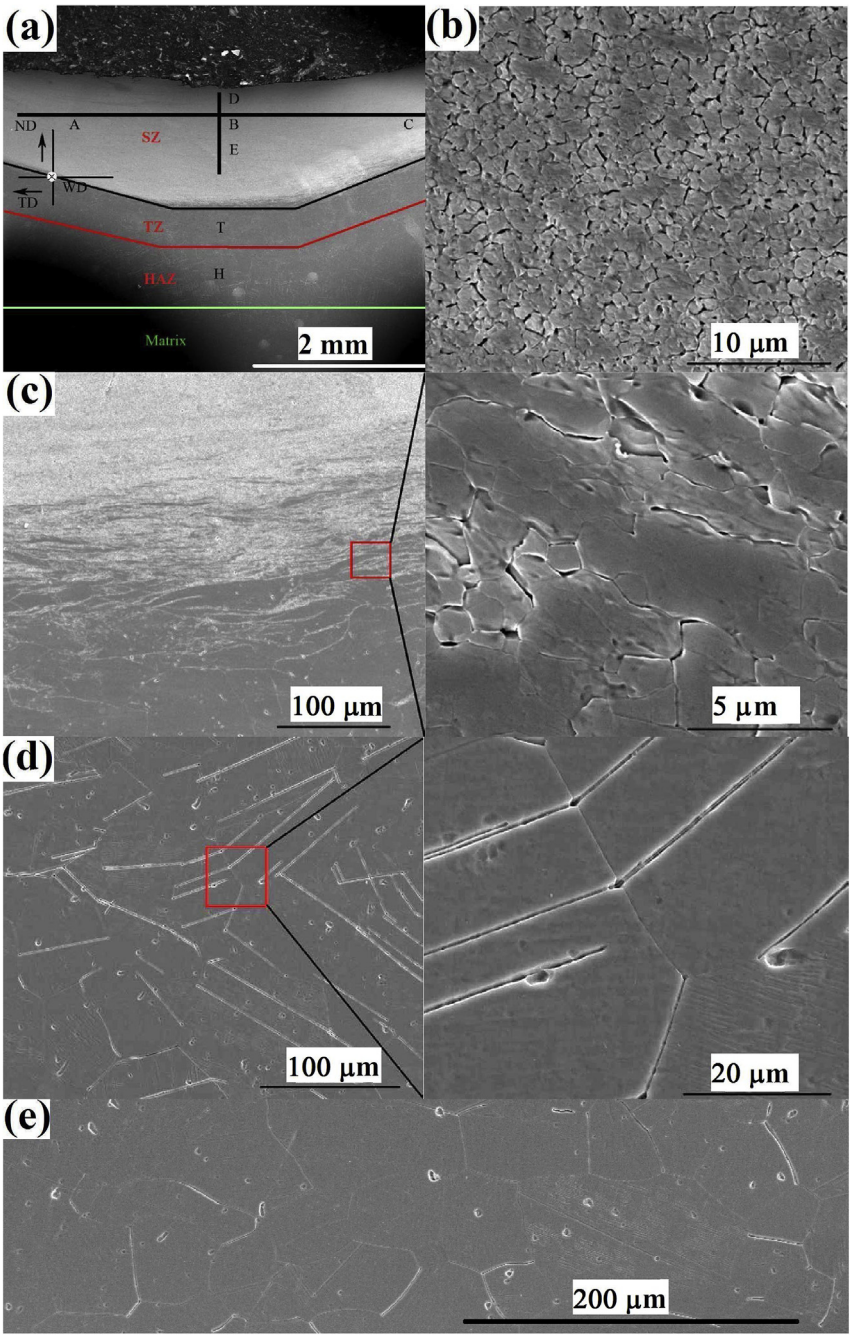

Fig. 2. SEM micrographs showing distinct regions in transversal cross-section of three-pass FSP-processed sample at a rotational speed of 300 r/min: (a) overview of different regions at a low magnification, and the enlarged views for (b) stir zone (SZ), (c) transition zone (TZ), (d) heat affected zone (HAZ), and (e) matrix. WD (welding direction), TD (transverse direction) and ND (normal direction) of the specimen are indicated. Note that there is no distinct difference in SEM images for A-E in (a).

of ω phase nucleation and the associated interface characteristics between β and ω phase is provided. Furthermore, zig-zag structured ω phase is clearly visible, showing ω in the $[11\bar{2}0]_\omega$ zone axis. Parallelogram structured β phase crystals along the $[1\bar{1}1]$ zone axis are also detected. The interface of zig-zag structure of ω phase region is not clear in atomic level but it shows a gradual change in the atomic structure transforming to β crystal structure. HRTEM image in enlarged regions directly show the diffuse spots of ω phase and β phase crystal, respectively. This is similar to the aged ω phase crystals in β-type titanium alloys [49], where zig-zag structure of stress-induced ω phase is also detected in β-type titanium alloy during FSP.

3.2. Superelasticity

Previous work on NiTi alloy *via* nanoindentation indicated that internal stresses required to induce martensitic transformation are comparable to the macroscopic critical transformation stresses [50]. Non-uniform stresses are obtained at the location where a very small volume of the material is indented during nanoindentation. Hence, an impression of the indenter tip equivalent to the unrecovered plastic deformation remains in the specimen after unloading. The recovered displacement includes both the elastic recovery and superelastic recovery [51].

Fig. 7 shows the schematic of nanoindentation test and strain

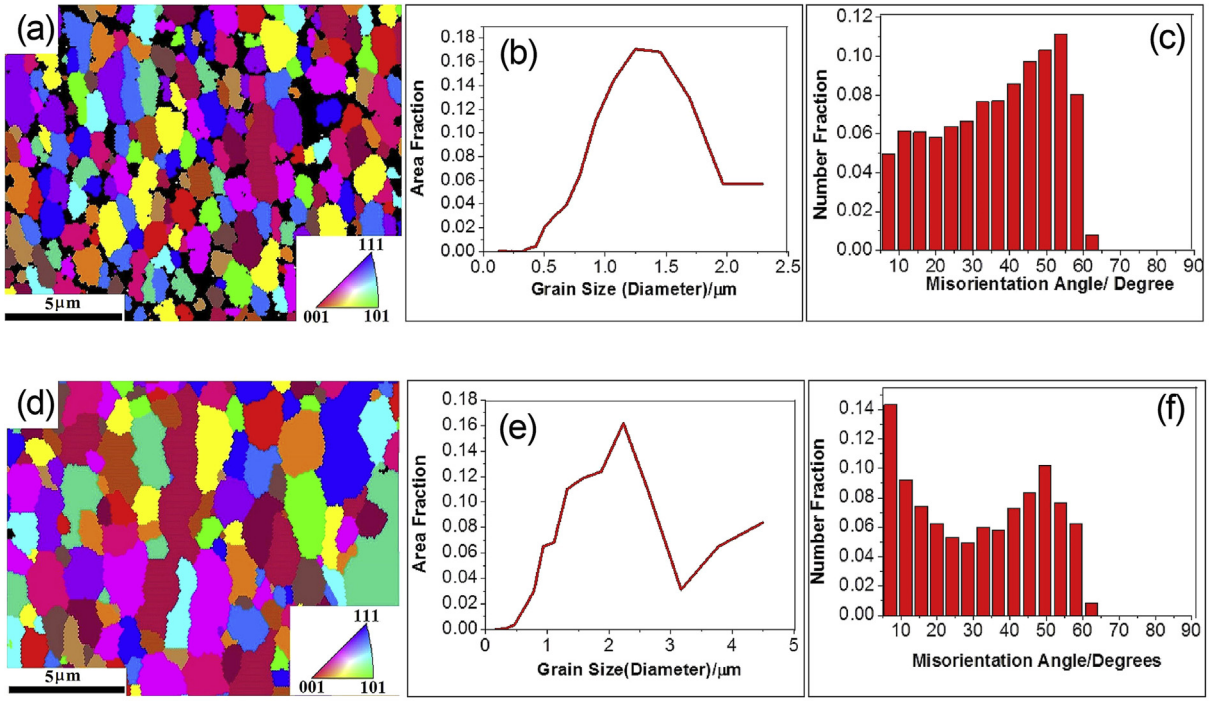

Fig. 3. EBSD maps of equiaxed grains for three-pass FSP-processed sample at a rotational speed of 300 r/min: (a) orientation map, (b) distribution of grain size and (c) misorientation angle distribution in stir zone (SZ), and (d) orientation map, (e) distribution of grain size and (f) misorientation angle distribution in transition zone (TZ).

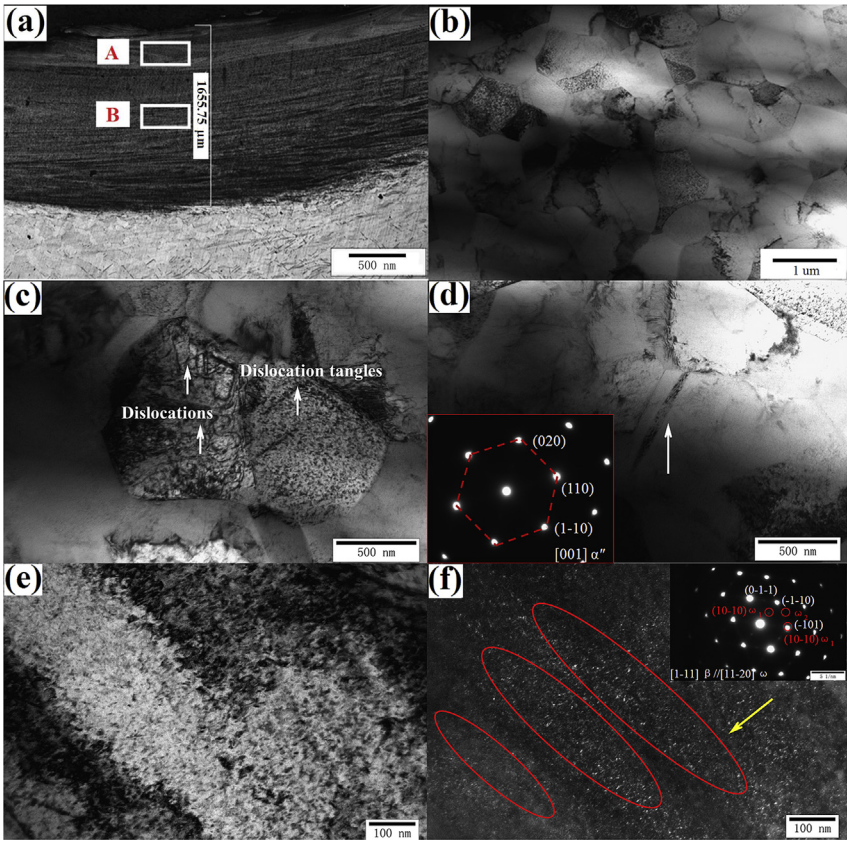

Fig. 4. Microstructure of the three-pass FSP-processed sample at rotation speed of 225 r/min: (a) optical image, and TEM images of (b) recrystallized grains in region A in stir zone, (c) recrystallized grains and dislocation tangles at high magnification, (d) martensite phase, (e) bright image of ω phase, (f) dark image of ω phase and the corresponding SAED pattern.

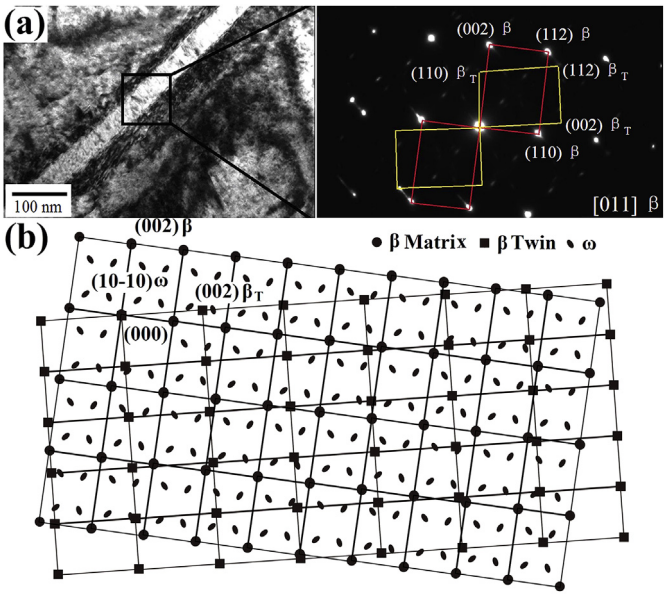

Fig. 5. TEM images in region A (Fig. 4 (a)) in stir zone for the three-pass FSP-processed sample at rotation speed of 225 r/min: (a) deformation twins corresponds to a <011> zone axis of the β phase and the corresponding SAED pattern; (b) indexed diagram corresponding to β matrix, β twin, and ω phase for (b).

recovery feature in the stir zone for the three-pass FSP-processed sample at rotation speed of 225 r/min. Fig. 7(a) and (b) show the indents in stir zone obtained consecutively from the up surface. Fig. 7(c) shows the load-depth curves of 51 indents in stir zone. The maximum indents depth (h_{max}), residual depth during unloading (h_r) associated with indents are shown in Fig. 7(d). We may define the elastic recovery $h_{er} = P_m/S$, with P_m and S being the maximum load and initial unloading slope respectively, and also the superelastic recovery $h_{sr} = h_{max}-h_r-P_m/S$. As such, the total strain recovery η_r, superelastic strain recovery η_{sr}, and elastic strain recovery η_{er} are:

$$\eta_r = (h_{max}-h_r)/h_{max} \quad (1)$$

$$\eta_{sr} = h_{sr}/h_{max} = (h_{max}-h_r-h_{er})/h_{max} \quad (2)$$

$$\eta_{er} = h_{er}/h_{max} \quad (3)$$

All the maximum depth (h_{max}), residual depth (h_r) and superelastic depth (h_{sr}) of the indentation vary from different indenter locals (Fig. 7(e)), which are considered as the main distinction of stress-induced martensite for individual indent. It is reported that higher total strain recovery indicates a better superelasticity, which is obtained in the condition that the stress required to induce martensite is lower than that for conventional plastic deformation in parent phase [52,53]. In this work, the loading-unloading cycles for three indentations, which were carried out in the location with the same depth to the surface, are quite reproducible for the same maximum load. Therefore, a selection of cycles is plotted for comparison. Comparing with different domains ranged from top surface in SZ towards the matrix (about 1530 μm in length), a highest η_r *of* 35.3% for indent 1 is obtained nearby the up surface. The total strain recovery decreases gradually when indents are located towards the middle region. However, a larger η_r (over 27%) is accessible for the indents from 42 to 51. In addition, a pronounced increase in maximum depth along with increased indent indicates the softening process from up surface of stir zone. Similar trend for superelastic strain recovery (η_{er}) is also observed clearly in Fig. 7(f).

4. Discussion

4.1. ω phase transformation in stir zone

So far, there exist two reported ω precipitation mechanisms. One is the shuffling mechanism associated with a thermally activated ω phase transformation, which has already been observed in group IV transition metals and alloys during heat treatment [54]. According to our knowledge, metastable ω phase transformation should be induced mainly by temperature increase and such athermal ω phase is present during quenching from the high temperature β phase region owing to a shuffling mechanism. However, in our previous work, no obvious athermal ω phase has been detected by increasing temperature followed by cooling from β phase region for Ti-35Nb-2Ta-3Zr alloy [29–32]. In this work, the temperature in the stir zone is detected around 900 °C by infrared temperature measuring instrument during FSP, which is higher than the β phase transformation temperature. Therefore, temperature increase has little effect on the metastable ω phase transformations after FSP, especially in stir zone. The other ω precipitation mechanism is the dislocation mechanism for deformation-induced ω phase transformation during deformation [55], which is induced mainly by internal stress. As reported in literature, internal stresses are important for microstructure evolution during thermo-mechanical treatment, as recovery and recrystallization are induced by heterogeneities in a deformed state, which are commonly associated with heterogeneities in dislocation formed during deformation [56]. As indicated in Ref. [57], deformation-induced ω phase is observed in nanocrystalline body-centered cubic (bcc) Mo during HPT. Also shock-induced ω phase was investigated in tantalum alloys [55]. In this work, nano-sized ω phase precipitates along grain boundaries and they distributes especially in recrystallized grains with several hundred nanometer in size (Fig. 4(e)). With increasing the depth towards matrix, the amount of ω phase induced in the middle stir zone becomes less while the grain size becomes smaller (Fig. 6(e)), which is similar to the deformation induced ω precipitation observed at the very beginning during tension in metastable β titanium alloy [58]. The present result is consistent with the previous work that the fraction of ω phase decreases monotonically with decreasing average grain size ranged in nanometer [59]. According to Ref. [55], the motion of partial 1/3[111] and 1/12[111] dislocations dissociated from the 1/2[111] whole dislocations contributes to the transition of β to ω. As reported in previous literature [60], any factor obstructing dislocation motion, such as through introducing high-density dislocation tangles and grain boundaries by cold rolling prior to aging, suppressing ω transformation, could assist in hindering the formation of ω.

However, the increase in α″ martensitic phase along with decrease in dislocation density is always accompanied by significant reducing the fraction of ω phase precipitation. As shown before, compared with the upper surface treated at a rotation speed of 225 r/min (Fig. 4(d)), much more deformation-induced α″ martensite is presented in the middle stir zone (Fig. 6(c)). ω phase precipitates are considered to be dissolved with increasing the deformation amount [58]. Currently, there was a speculation that the structural change from ω to α″ is more difficult to achieve comparing with the transformation from β to α″, which is ascribed to the decrease in the amount of ω phase [61]. However, little experimental evidence could prove this speculation. In this work, the dissolving of ω phase is discussed in detail for the specimens with different rotation speeds as indicated in Fig. 8.

It can be observed that most dislocations glide in slip bands for both specimens FSP-processed at different rotation speed as marked by yellow arrows in Fig. 8(a) and (b). Several single

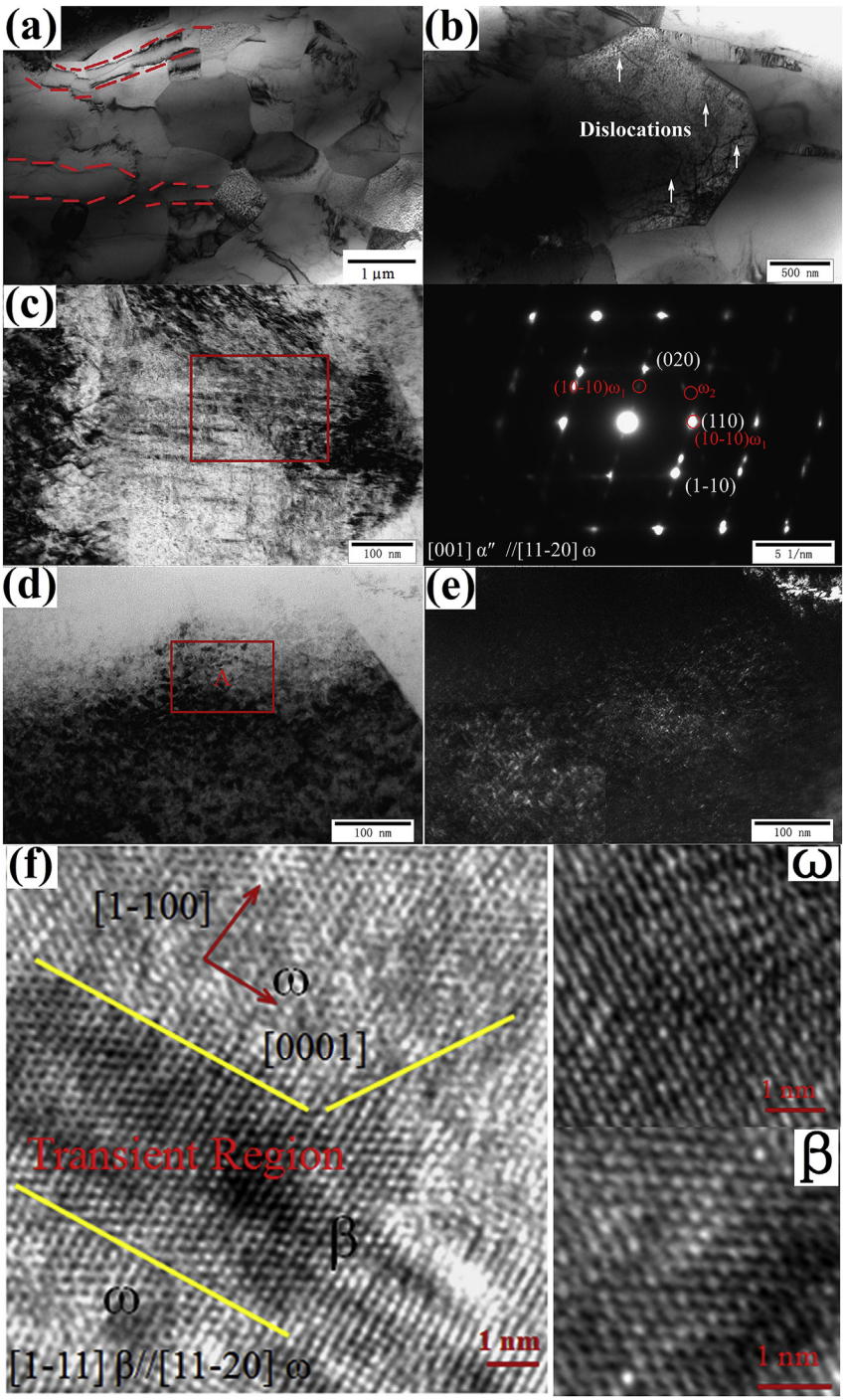

Fig. 6. TEM images of region B indicated in Fig. 4(a) in stir zone for the three-pass FSP-processed sample at rotation speed of 225 r/min: (a) recrystallized grains, (b) recrystallized grains with dislocation tangles around grain boundary at high magnification, (c) martensitic phase along $<001>_{\alpha''}$ zone axis, ω phase along $<11\bar{2}0>_{\omega}$ direction and its corresponding SAED pattern, (d) bright image of ω phase, (e) dark image of ω phase, (f) HRTEM image of domain A in (d) along $<1\bar{1}1>$ β zone axis showing the boundary between ω phase and β phase, including the complete collapse of atomic planes in ω precipitates along $<11\bar{2}0>_{\omega}$ direction.

dislocations glide in the grain and slip planes are distinguished from slip traces left by dislocations at the sample surfaces (indicated by white arrows). Due to multiple dislocation slips, some slip traces are wavy, while other traces are straight. Same scenario was also clearly reported in Ref. [62]. Compared with the FSP-processed specimen at a rotation speed of 225 r/min, many more slip bands accompanying with dislocation tangles are present in the specimen at the speed of 300 r/min, as indicated in Fig. 8(b), which is attributed to much larger deformation extent at higher rotation speed. Thus, metastable ω phase dissolving feature is evident in the region where dislocations gliding is present, especially in the specimen processed at a higher rotation speed (Fig. 8 (b)). After considering that the observed areas possess the same thickness for both specimens, we compare the HRTEM images for these specimens as shown in Fig. 8(c) and (d). In the current work, the details for the domains of ω dissolving show clearly the transformation from ω phase to β phase. Many more ω precipitates are firstly promoted accompanying with a few ω dissolving regions and

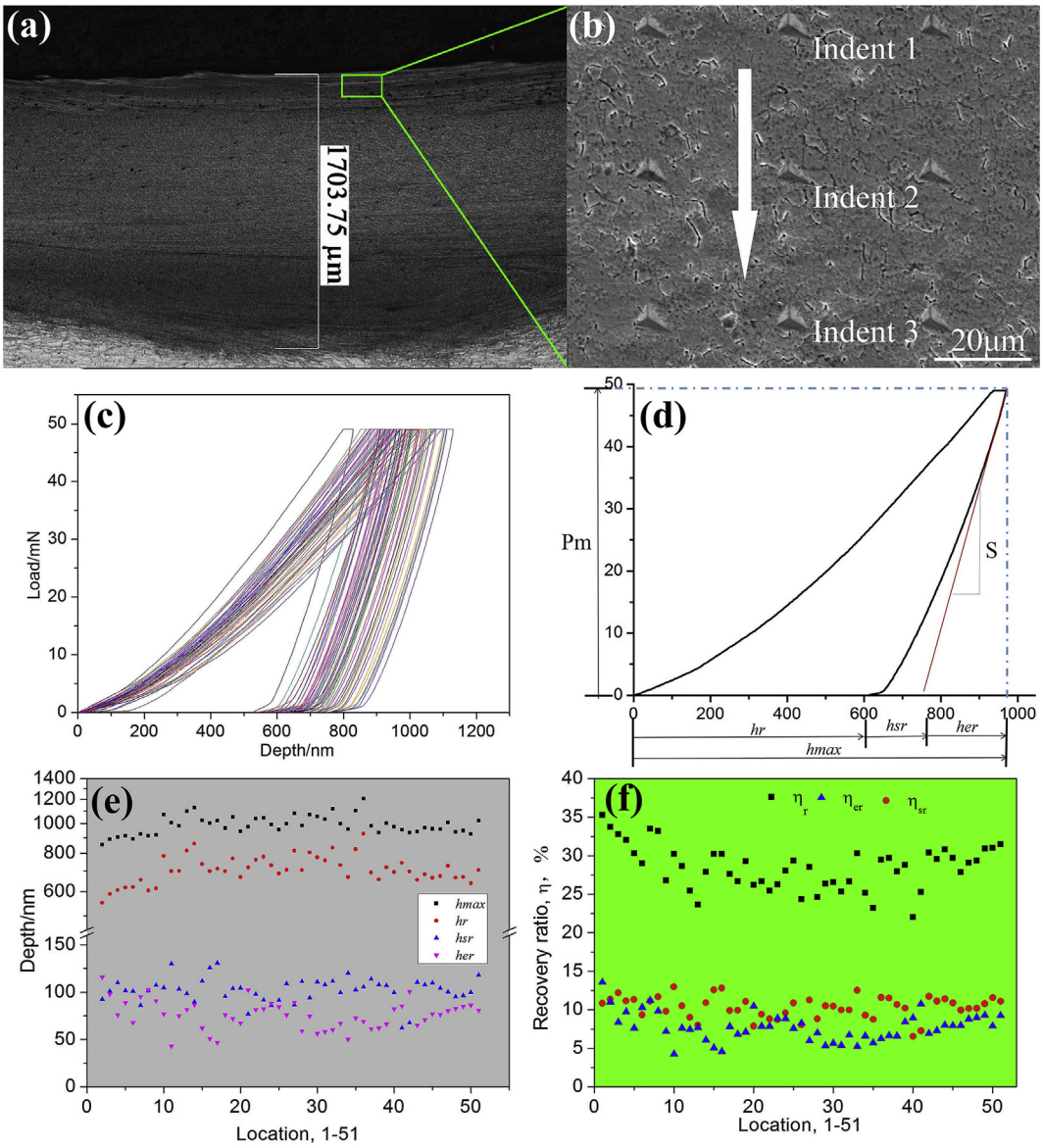

Fig. 7. Schematic of nanoindentation test and strain recovery feature in the stir zone for the three-pass FSP-processed sample at rotation speed of 225 r/min: (a) and (b) indents in stir zone obtained orderly from the up surface (the sequence of numbers correspond to indents starting from the top surface), (c) load-displacement curves obtained from the 51 indents, (d) load-displacement curve for solution-treated specimen, (e) maximum indents depth (h_{max}), residual depth during unloading (h_r), elastic recovery (h_{er}) *and* superelastic recovery (h_{sr}) associated with indents, (f) total strain recovery (η_r), superelastic strain recovery (η_{sr}), and elastic strain recovery (η_{er}) associated with indents.

gradually disappear with increasing the rotation speed from 225 r/min to 300 r/min. As seen from Fig. 8(d), many more domains containing β phase appear and more feature of ω dissolving is observed clearly, which is promoted by dislocation gliding. Fig. 8 (e) shows the indexed diagram corresponding to β phase and ω phase.

Fig. 9 shows the schematic view of microstructural characteristics in SZ, TZ, HAZ and BM, accompanying ω phase transformation. The detailed ω phase transformation mechanism is shown in Fig. 9 (b). During severe plastic deformation, especially for the upper surface at a rotation speed of 300 r/min, much more vacancies are formed owing to the increased dislocation slipping, accelerating ω phase dissolving, as clearly indicated in Fig. 9. During this process, a homogeneous lattice deformation and lattice invariant shears are also observed. It was reported [63] that the vacancy mediated atom diffusion normally has a lower energy barrier which promotes the phase transformation from ω phase to α phase. In the current work, vacancy-ordered metastable ω phase dissolves and finally develops to the β precipitates, transforming $[11\bar{2}0]_\omega$ phase orientation to the $[1\bar{1}1]_\beta$ directly. Fig. 10 shows the XRD patterns of the specimens for both the upper surface and surface in SZ at a rotation speed of 300 r/min. ω phase is observed in the upper surface, which can be indicated clearly in the enlarged XRD pattern in Fig. 10 inset. In contrast, both the α″ martensite and β parent phases are observed in the upper surface and surface in SZ. The intensity of the (020) peak for β phase is enhanced with the gradually increasing the depth from upper surface to surface, implying that much more α″ martensite transformation appears in surface accompanying disappearance of ω phase. This is consistent with the previous discussion in Fig. 9(b).

4.2. Superelasticity in stir zone

The enlarged load-displacement curves in nanoindentation experiments indicate the typical behavior of superelasticity of FSP-

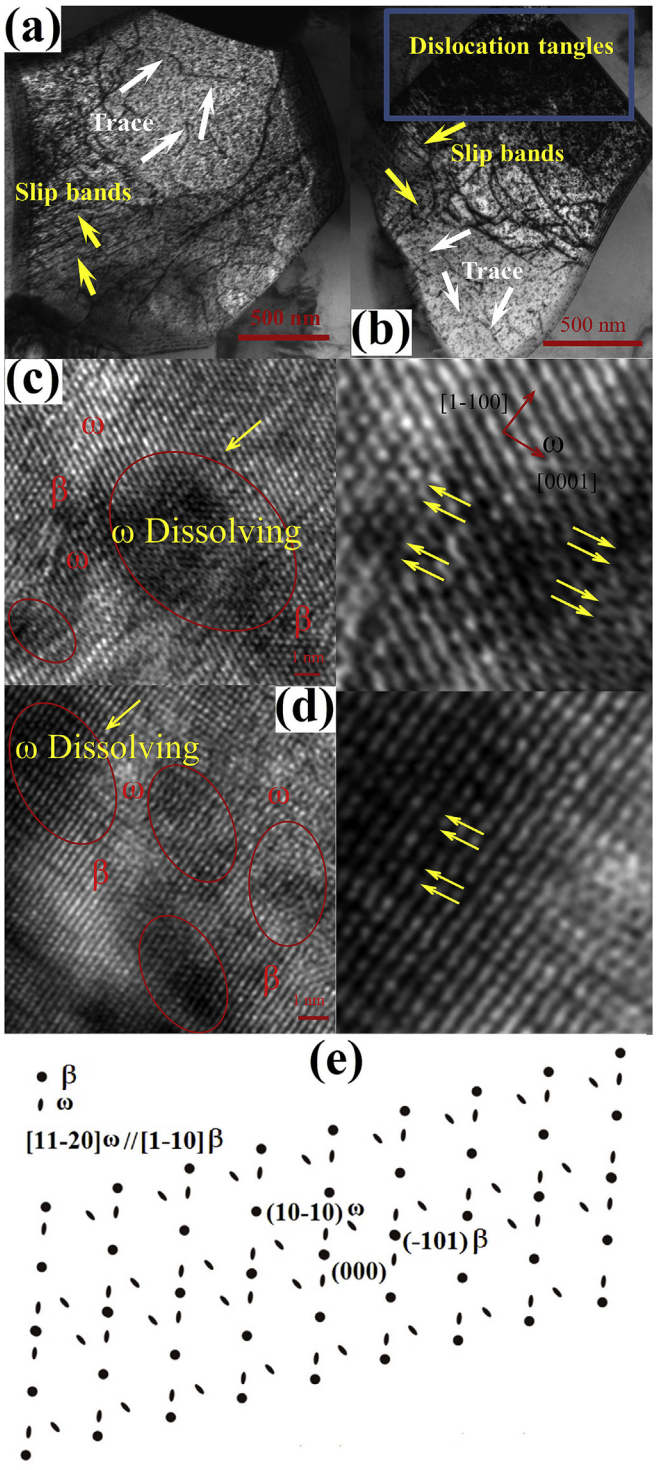

Fig. 8. TEM and HRTEM images of the stir zone for the three-pass FSP-processed sample at varied rotation speeds: (a) Slip bands and slip traces of single dislocations (trace) for the specimen FSP-processed at 225 r/min. (b) Slip bands and slip traces of single dislocations (trace) for the specimen FSP-processed at 300 r/min. (c) HRTEM image at 225 r/min and (d) HRTEM image at 300 r/min, (e) the indexed diagram corresponding to β phase and ω phase.

processed specimens (Fig. 11). To achieve the same indentation depths, distinct load should be applied to the samples. For example, when the indentation depth is 700 nm, the highest load is around 37, 33, 30, 33, and 30 mN for indent 1, 17, 32, 42 and 51, respectively. The highest values in hardness appear in indent 1 to indent 8, as

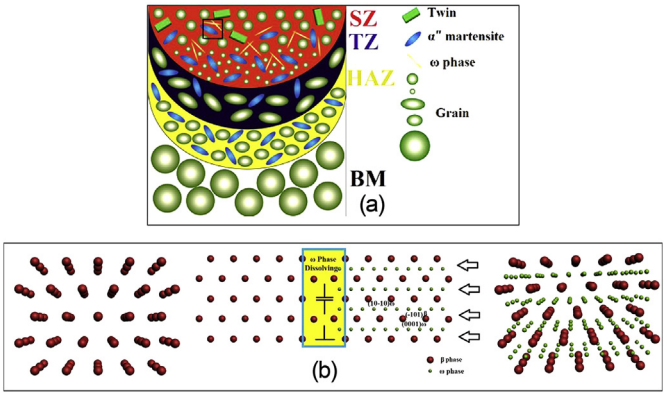

Fig. 9. Schematic view of microstructural characteristics in different regions: (a) in SZ, TZ, HAZ and BM, (b) ω phase transformation.

indicated in Fig. 11(f). Meanwhile, among all the 51 indents, the highest value in elastic modulus, which is presented by the slope of $P(h)$ curve after unloading, is also achieved in indent 1. As seen from the value of the recovery ratio in Fig. 7(f), the maximum value of the recovery ratio is obtained for indent 1, which is attributed primarily to the reverse transformation of deformation-induced martensitic transformation, similar to Refs. [64,65]. By increasing indent number towards the transition zone (i.e. the indent locale gradually closer to the transition zone) leads to that much more martensites nucleate, which re-orientate during nanoindentation testing. Therefore, lower load is applied compared with those in the upper surface (Fig. 11(b)-(e)), resulting in a gradual decrease in both elastic modulus and hardness (Fig. 11(f)). It can be proved that martensite nucleation and its reverse transformation occur easily in the region towards transition zone according to the record that the highest recovery ratio (Fig. 7(f)) and lower elastic modulus and hardness are achieved in indent 51, the nearest position to transition zone. The pop-ins on the load-displacement curve corresponds to the deformation-induced martensitic transformation, which was previously discussed in Ref. [66]. Ahn et al. [66] also attributed the first pop-in event to the dislocation nucleation in TRIP steels followed by martensitic transformation. Among all the mentioned indents in Fig. 11, the first pop-in with highest load occurs at indent

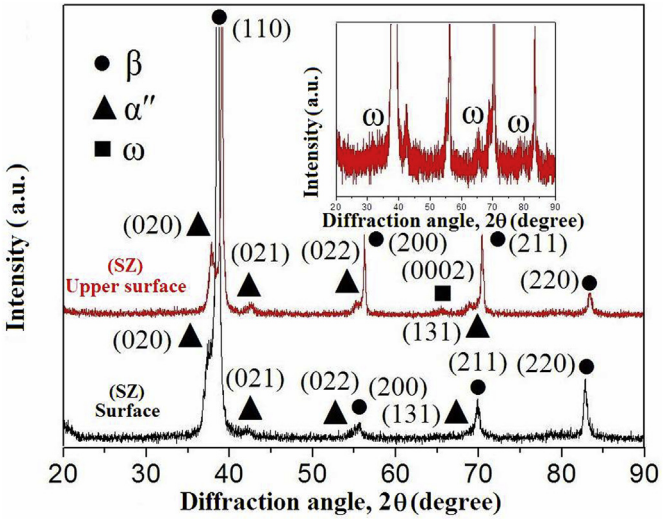

Fig. 10. XRD patterns of the specimens for both the upper surface and surface in SZ at a rotation speed of 300 r/min.

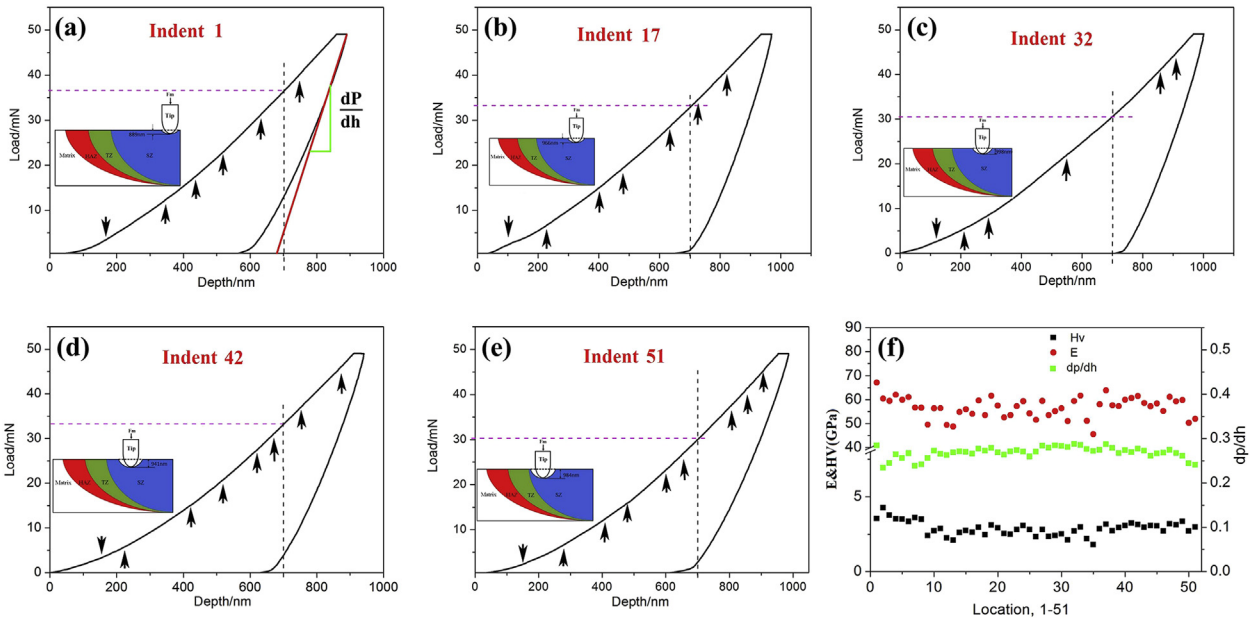

Fig. 11. Nanoindentation experiments conducted with Berkovich indent: (a) indent 1, (b) indent 17, (c) indent 32, (d) indent 42, (e) indent 51, (f) relationship between the slope of P(h) curve, hardness, elastic modulus and different indents. The numbers correspond to the sequence of indents starting from the top surface in stir zone. The positions of the pop-ins are arrowed.

1, seen from the enlarged image inside (Fig. 11(a)), which is consistent with the hardening effect for indent 1. On the other hand, many more pop-ins presenting in indent 51 also provide solid evidence that much more martensitic transformation is achieved at this location.

To further indicate the deformation features during nanoindentation testing, series of scanning electron microscopy (SEM) images of remnant nanoindents (maximal applied load of 50 mN) are shown in Fig. 12. Fig. 12(a) shows the schematic representation of residual indentation area including dislocation and martensite transformation feature during nanoindentation. As discussed above, the recovered displacement includes both the elastic recovery (h_{er}) and superelastic recovery (h_{sr}), observed in Fig. 12(a). Similar morphology of indent left after unloading is achieved with different Berkovich tip geometry. Anisotropy of the geometry size for indent 1 is considered as the result from the inhomogeneous nucleation of deformation-induced martensite, accompanying with dislocations. Obvious cracks between grain boundaries are observed. The largest superelasticity obtained in indent 1, as indicated in Fig. 7(e) and (f), is attributed to the precipitation hardening effect of much more fine ω phase and fine grain strengthening after FSP, which is caused by increasing critical stress for slip deformation. With increase in indent number, isotropic geometry sizes for indents 17, 32, and 42 are achieved which show a homogenous nucleation of deformation-induced martensite, as indicated in Fig. 12(c–e). As for both indents 42 and 51 (Fig. 12(f)), towards

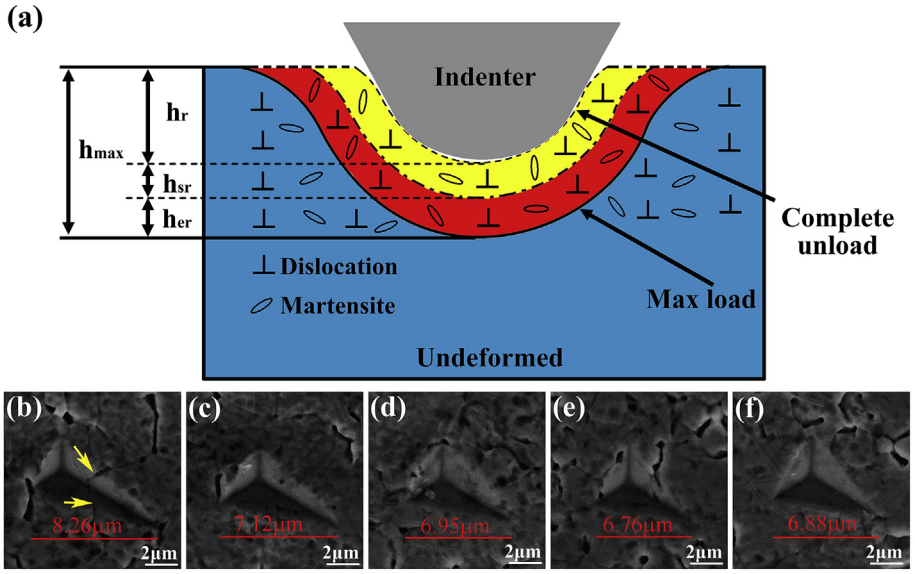

Fig. 12. Series of SEM images of remnant nanoindents (maximal applied load of 50 mN): (a) schematic representation of residual indentation area including dislocation and martensite, (b) indent 1, (c) indent 17, (d) indent 32, (e) indent 42, (f) indent 51.

transition zone, where martensite nucleation and its reverse transformation occur easily, anisotropy of the geometry size is obtained with smallest remnant nanoindents.

5. Conclusion

(1) Transition zone (TZ) consists of coarser grains than stir zone (SZ). Different from the microstructure in SZ and TZ, a large number of martensites including micro-twinning are presented in region of heat affected zone (HAZ). The morphology and distribution of martensite in HAZ are significantly different compared to those of SZ and TZ.

(2) The high fraction of high angle grain boundaries (HAGBs) implies that dynamic recrystallization (DRX) occurs during FSP due to severe plastic deformation for three passes and the average misorientation angle is 36.2°. Compared with the microstructure evolution in SZ, relatively large grain size can be observed in TZ, which ranged around 1.2 μm. Meanwhile, the fraction of HAGBs in TZ is 76.4% and the average misorientation angle is 31.4°. As clearly clarified, β grains are homogeneously refined from TZ to SZ accompanying the increase in the average misorientation angle.

(3) After thorough recrystallization, the existing dislocations gradually arrange themselves at sub-grain boundaries, and the increase in sub-grain boundary misorientation angle ultimately promotes the formation of high angle grain boundary. Recrystallization is obtained accompanying dislocation annihilation while with just a few discontinuous dislocation lines appearing in the recrystallized grains.

(4) Zig-zag structured stress-induced ω phase is also detected in β titanium alloy during FSP. In addition, stress-induced α″ phase also precipitates accompanying ω phase nucleation and dislocation annihilation. The process of ω dissolving is promoted by the dislocation gliding.

(5) With increasing indent number towards the transition zone, much more martensites nucleate, which re-orientate during nanoindentation test, resulting in gradual decrease in both elastic modulus and hardness.

Acknowledgements

The authors would like to acknowledge the financial supports provided by National Science Foundation under Grant No. 51302168, 51674167, Shanghai Pujiang Program under Grant No. 15PJD017, Medical Engineering Cross Research Foundation of Shanghai Jiao Tong University under grant No. YG2014MS02, Shanghai Jiao Tong University Chenxing Program under Grant No. 15X100080069.

References

[1] S. Ehtemam Haghighi, H.B. Lu, G.Y. Jian, G.H. Cao, D. Habibi, L.C. Zhang, Effect of α″ martensite on the microstructure and mechanical properties of beta-type Ti-Fe-Ta Alloys, Mater. Des. 76 (2015) 47–54.
[2] L.C. Zhang, D. Klemm, J. Eckert, Y.L. Hao, T.B. Sercombe, Manufacture by selective laser melting and mechanical behavior of a biomedical Ti-24Nb-4Zr-8Sn alloy, Scr. Mater. 65 (2011) 21–24.
[3] L.Q. Wang, W.J. Lu, J.N. Qin, F. Zhang, D. Zhang, The characterization of shape memory effect for low elastic modulus biomedical beta-type titanium alloy, Mater. Charact. 61 (2010) 535–541.
[4] E.G. Obbard, Y.L. Hao, T. Akahori, R.J. Talling, M. Niinomi, D. Dye, R. Yang, Mechanics of superelasticity in Ti-30Nb-(8-10)Ta-5Zr alloy, Acta Mater. 58 (2010) 3557–3567.
[5] R.J. Talling, R.J. Dashwood, M. Jackson, D. Dye, On the mechanism of superelasticity in Gum metal, Acta Mater. 57 (2009) 1188–1198.
[6] H.Y. Kim, Y. Ikehara, J.I. Kim, H. Hosoda, S. Miyazaki, Martensitic transformation, shape memory effect and superelasticity of Ti–Nb binary alloys, Acta Mater. 54 (2006) 2419–2429.
[7] H.Y. Kim, H. Satoru, J.I. Kim, H. Hosoda, S. Miyazaki, Mechanical properties and shape memory behavior of Ti-Nb alloys, Mater Trans. 45 (2004) 2443–2448.
[8] L.S. Toth, C.F. Gu, Ultrafine-grain metals by severe plastic deformation, Mater. Charact. 92 (2014) 1–14.
[9] C.Y. Zhu, Y.T. Lv, C. Qian, H.X. Qian, T. Jiao, L.Q. Wang, F.Q. Zhang, Proliferation and osteogenic differentiation of rat BMSCs on a novel Ti/SiC metal matrix nanocomposite modified by friction stir processing, Sci. Rep. 38875 (2016) pp.1–15.
[10] W. Xu, X. Wu, M. Calin, M. Stoica, J. Eckert, K. Xia, Formation of an ultrafine-grained structure during equal-channel angular pressing of a β-titanium alloy with low phase stability, Scr. Mater. 60 (2009) 1012–1015.
[11] Z.J. Lin, L.Q. Wang, X.B. Xue, W.J. Lu, J.N. Qin, D. Zhang, Microstructure evolution and mechanical properties of a Ti-35Nb-2Ta-3Zr biomedical alloy processed by equal channel angular pressing (ECAP), Mater. Sci. Eng. C 33 (2013) 4551–4561.
[12] H. Yilmazer, M. Niinomi, K. Cho, M. Nakai, J. Hieda, S. Sato, Y. Todaka, Microstructural evolution of precipitation-hardened β-type titanium alloy through high-pressure torsion, Acta Mater. 80 (2014) 172–182.
[13] H. Yilmazer, M. Niinomi, M. Nakai, K. Cho, J. Hieda, Y. Todaka, T. Miyazaki, Mechanical properties of a medical β-type titanium alloy with specific microstructural evolution through high-pressure torsion, Mater. Sci. Eng. C 33 (2013) 2499–2507.
[14] K. Edalati, Z. Horita, H. Fujiwara, K. Ameyama, Cold consolidation of ball-milled titanium powders using high-pressure torsion, Metall. Mater. Trans. A 41 (2010) 3308–3317.
[15] C.T. Wang, N. Gao, M.G. Gee, R.J.K. Wood, T.G. Langdon, Effect of grain size on the micro-tribological behavior of pure titanium processed by high-pressure torsion, Wear 280 (2012) 28–35.
[16] A. Balyanov, J. Kutnyakova, N.A. Amirkhanova, V.V. Stolyarov, R.Z. Valiev, X.Z. Liao, Y.H. Zhao, Y.B. Jiang, H.F. Xu, T.C. Lowe, Y.T. Zhu, Corrosion resistance of ultra fine-grained Ti, Scr. Mater. 51 (2004) 225–229.
[17] R.Z. Valiev, I. Sabirov, A.P. Zhilyaev, T.G. Langdon, Bulk nanostructured metals for innovative applications, JOM 64 (2012) 1134–1142.
[18] B.B. Straumal, A.S. Gornakova, A.A. Mazilkin, O.B. Fabrichnaya, M.J. Kriegel, B. Baretzky, J.Z. Jiang, S.V. Dobatkin, Phase transformations in the severely plastically deformed Zr–Nb alloys, Mater. Lett. 81 (2012) 225–228.
[19] F.C. Ma, S. Chen, P. Liu, F. Geng, W. Li, X.K. Liu, D.H. He, D. Pan, Improvement of β-TCP/PLLA biodegradable material by surface modification with stearic acid, Mater. Sci. Eng. C 62 (2016) 407–413.
[20] L. Zhang, H.F. Zhang, W.Q. Li, T. Gemming, Z.W. Zhu, H.M. Fu, J. Eckert, S. Pauly, Negentropic stabilization of metastable β-Ti in bulk metallic glass composites, Scr. Mater. 125 (2016) pp.19–23.
[21] C.W. Chan, S. Lee, G. Smith, G. Sarri, C.H. Ng, A. Sharba, H.C. Man, Enhancement of wear and corrosion resistance of beta titanium alloy by laser gas alloying with nitrogen, Appl. Surf. Sci. 367 (2016) 80–90.
[22] S.J. Li, R. Yang, S. Li, Y.L. Hao, Y.Y. Cui, M. Niinomi, Z.X. Guo, Wear characteristics of Ti–Nb–Ta–Zr and Ti–6Al–4V alloys for biomedical applications, Wear 257 (2004) 869–876.
[23] M. Niinomi, Mechanical properties of biomedical titanium alloys, Mater. Sci. Eng. A 243 (1998) 231–236.
[24] G. Manivasagam, U.K. Mudali, R. Asokamani, B. Raj, Influence of thermo-mechanical processing on microstructure, mechanical properties and corrosion behavior of a new metastable β-titanium biomedical alloy, Bull. Mater. Sci. 38 (2015) pp.247–258.
[25] R.S. Mishra, Z. Ma, I. Charit, Friction stir processing: a novel technique for fabrication of surface composite, Mater. Sci. Eng. A 341 (2003) 307–310.
[26] R. Sathiskumar, N. Murugan, I. Dinaharan, S. Vijay, Prediction of mechanical and wear properties of copper surface composites fabricated using friction stir processing, Mater. Des. 55 (2014) 224–234.
[27] A.H. Feng, Z.Y. Ma, Enhanced mechanical properties of Mg–Al–Zn cast alloy via friction stir processing, Scr. Mater. 56 (2007) 397–400.
[28] M. Atapour, A. Pilchak, G. Frankel, J. Williams, Corrosion behaviour of investment cast and friction stir processed Ti-6Al-4V, Corros. Sci. 52 (2010) 3062–3069.
[29] L.Q. Wang, W.J. Lu, J.N. Qin, F. Zhang, D. Zhang, Texture and superelastic behavior of cold-rolled TiNbTaZr alloy, Mater. Sci. Eng. A 491 (2008) 372–377.
[30] L.Q. Wang, W.J. Lu, J.N. Qin, F. Zhang, D. Zhang, Influence of cold deformation on martensite transformation and mechanical properties of Ti–Nb–Ta–Zr alloy, J. Alloys Compd. 469 (2009) 512–518.
[31] L.Q. Wang, W.J. Lu, J.N. Qin, F. Zhang, D. Zhang, Effect of precipitation phase on microstructure and superelasticity of cold-rolled beta titanium alloy during heat treatment, Mater. Des. 30 (2009) 3873–3878.
[32] L.Q. Wang, W.J. Lu, J.N. Qin, F. Zhang, D. Zhang, Change in microstructures and mechanical properties of biomedical Ti-Nb-Ta-Zr system alloy through cross-rolling, Mater. Trans. 49 (2008) 1791–1795.
[33] S.H. Kim, S. Jin Kang, M.H. Park, C.W. Yang, H.C. Lee, H.N. Han, M.Y. Kim, Vacancy-mediated ω-assisted α-phase formation mechanism in titanium–molybdenum alloy, Acta Mater. 83 (2015) 499–506.
[34] Z.H. Ding, C.J. Zhang, L.C. Xie, L.C. Zhang, L.Q. Wang, W.J. Lu, Effects of friction stir processing on the phase transformation and microstructure of TiO2 compounded Ti-6Al-4V alloy, Metall. Mater. Trans. A 47 (2016) 5675–5679.
[35] S. Mironov, Y.S. Sato, H. Kokawa, Microstructural evolution during friction stir-processing of pure iron, Acta Mater. 56 (2008) 2602–2614.
[36] P.B. Prangnell, C.P. Heason, Grain structure formation during friction stir welding observed by the “stop action technique”, Acta Mater. 53 (2005) 3179–3192.

[37] R.W. Fonda, J.F. Bingert, K.J. Colligan, Development of grain structure during friction stir welding, Scr. Mater. 51 (2004) 243–248.
[38] Yutaka S. Sato, Tracy W. Nelson, Colin J. Sterling, Recrystallization in type 304L stainless steel during friction stirring, Acta Mater. 53 (2005) 637–645.
[39] Z.Y. Ma, R.S. Mishra, M.W. Mahoney, Superplastic deformation behaviour of friction stir processed 7075Al alloy, Acta Mater. 50 (2002) 4419–4430.
[40] A. Zafari, X.S. Wei, W. Xu, K. Xia, Formation of nanocrystalline β structure in metastable beta Ti alloy during high pressure torsion: the role played by stress induced martensitic transformation, Acta Mater. 97 (2015) pp.146–155.
[41] Y. Ren, F.C. Wang, C.W. Tan, S.Y. Wang, X.D. Yu, J.W. Jiang, H.N. Cai, J. Alloy. Compd. 578 (2013) 547–552.
[42] L.H. Wu, D. Wang, B.L. Xiao, Z.Y. Ma, Microstructural evolution of the thermomechanically affected zone in a Ti–6Al–4V friction stir welded joint, Scr. Mater. 78–79 (2014) 17–20.
[43] Y. Cao, Y.B. Wang, X.H. An, X.Z. Liao, M. Kawasaki, S.P. Ringer, T.G. Langdon, Y.T. Zhu, Grain boundary formation by remnant dislocations from the detwinning of thin nano-twins, Scr. Mater. 100 (2015) 98–101.
[44] N. Sakaguchi, M. Niinomi, T. Akahori, Deformation behaviors of Ti-Nb-Ta-Zr system alloys for biomedical applications, Mater. Trans. 45 (2004) 1113–1119.
[45] S. Hanada, Correlation of tensile properties, deformation modes, and phase stability in commercial β-phase titanium alloys, Metall. Trans. A 18 (1987) 265–271.
[46] Y. Yang, G.P. Li, H. Wang, S.Q. Wu, L.C. Zhang, Y.L. Li, K. Yang, Formation of zigzag-shaped {112}< 111> β mechanical twins in Ti–24.5 Nb–0.7 Ta–2 Zr–1.4 O alloy, Scr. Mater. 66 (2012) 211–214.
[47] R.S. Mishra, Z. Ma, Friction stir welding and processing, Mater. Sci. Eng. R. 50 (2005) 1–78.
[48] L. Murr, Y. Li, R. Flores, E.A. Trillo, J. McClure, Intercalation vortices and related microstructural features in the friction-stir welding of dissimilar metals, Mater. Res. Innov. 2 (1998) 150–163.
[49] E. Sukedai, Y. Kitano, A. Ohnishi, Investigation of initial structures of aged ω phase crystals in β titanium alloys using high resolution electron microscopy, Micron 28 (1997) 259–277.
[50] C.P. Frick, T.W. Lang, K. Spark, K. Gall, Stress-induced martensitic transformations and shape memory at nanometer scales, Acta Mater. 54 (2006) 2223–2234.
[51] Z. Sun, S. Van Petegem, A. Cervellino, K. Durst, W. Blum, H. Van Swygenhoven, Dynamic recovery in nanocrystalline Ni, Acta Mater. 91 (2015) 112–127.
[52] A.J. Muir Wood, T.W. Clyne, Measurement and modelling of the nanoindentation response of shape memory alloys, Acta Mater. 54 (2006) 5607–5615.
[53] K. Otsuka, C.M. Wayman, Mechanism of shape memory effect and superelasticity, Shape Mem. Mater. (1998) 27–48.
[54] S.K. Sikka, Y.K. Vohra, R. Chidambaram, Omega phase in materials, Prog. Mater. Sci. 27 (1982) 245–310.
[55] L.M. Hsiung, D.H. Lassila, Shock-induced deformation twinning and omega transformation in tantalum and tantalum–tungsten alloys, Acta Mater. 48 (2000) 4851–4865.
[56] R. Hoppe, F. Appel, Deformation-induced internal stresses in multiphase titanium aluminide alloys, Acta Mater. 64 (2014) 169–178.
[57] G.M. Cheng, H. Yuan, W.W. Jian, W.Z. Xu, P.C. Millett, Y.T. Zhu, Deformation-induced ω phase in nanocrystalline Mo, Scr. Mater. 68 (2013) 130–133.
[58] F. Sun, J.Y. Zhang, M. Marteleur, T. Gloriant, P. Vermaut, D. Laillé, P. Castany, C. Curfs, P.J. Jacques, F. Prima, Investigation of early stage deformation mechanisms in a metastable β titanium alloy showing combined twinning-induced plasticity and transformation-induced plasticity effects, Acta Mater. 61 (2013) 6406–6417.
[59] K. Edalati, T. Daio, M. Arita, S. Lee, Z. Horita, A. Togo, et al., High-pressure torsion of titanium at cryogenic and room temperatures: grain size effect on allotropic phase transformations, Acta Mater. 68 (2014) 207–213.
[60] S. Guo, Q.K. Meng, L. Hu, G.Y. Liao, X.Q. Zhao, H.B. Xu, Suppression of isothermal ω phase by dislocation tangles and grain boundaries in metastable β-type titanium alloys, J. Alloys Compd. 550 (2013) pp.35–38.
[61] Y. Ohmori, T. Ogo, K. Nakai, S. Kobayashi, Effects of ω-phase precipitation on β→ α, α″ transformations in a metastable β titanium alloy, Mater. Sci. Eng. A 312 (2001) 182–188.
[62] M. Besse, P. Castany, T. Gloriant, Mechanisms of deformation in gum metal TNTZ-O and TNTZ titanium alloys: a comparative study on the oxygen influence, Acta Mater. 59 (2011) 5982–5988.
[63] S.H. Kim, S.J. Kang, M.H. Park, C.W. Yang, H.C. Lee, H.N. Han, et al., Vacancy-mediated ω-assisted α-phase formation mechanism in titanium–molybdenum alloy, Acta Mater. 83 (2015) 499–506.
[64] J. Pfetzing-Micklich, C. Somsen, A. Dlouhy, C. Begau, A. Hartmaier, F.X. Wagner, et al., On the crystallographic anisotropy of nanoindentation in pseudoelastic NiTi, Acta Mater. 61 (2013) 602–616.
[65] W.C. Oliver, G.M. Pharr, An improved technique for determining hardness and elastic modulus using load and displacement sensing indentation experiments, J. Mater. Res. Home 7 (1992) 1564–1583.
[66] T.H. Ahn, C.S. Oh, D.H. Kim, K.H. Oh, H. Bei, E.P. George, H.N. Han, Investigation of strain-induced martensitic transformation in metastable austenite using nanoindentation, Scr. Mater. 63 (2010) 540–543.